Numerical simulation research on the overturning of gantry crane by downbursts

Jia-Chen Su [a], Lei Li [a,b,c,*], Pak Wai Chan [d], Qian-Jin Zhou [a], Hong-Long Yang [e]

[a] *School of Atmospheric Sciences, Sun Yat-Sen University and Southern Marine Science and Engineering Guangdong Laboratory (Zhuhai), Zhuhai, 519082, China*
[b] *Guangdong Provincial Observation and Research Station for Climate Environment and Air Quality Change in the Pearl River Estuary, Zhuhai, 519082, China*
[c] *Key Laboratory of Tropical Atmosphere-Ocean System (Sun Yat-sen University), Ministry of Education, Zhuhai, 519082, China*
[d] *Hong Kong Observatory, Kowloon, Hong Kong, 999077, China*
[e] *Shenzhen National Climate Observatory, Shenzhen, 518040, China*

A R T I C L E I N F O

Keywords:
Downburst
Vertical profile of wind speed
Gantry crane
Computational fluid dynamics (CFD)
Fluid-structure interaction

A B S T R A C T

Based on the simulation of the fluid-structure interaction response, the cause of an overturning of a gantry crane induced by a downburst in Shenzhen is studied in this paper. According to the results, (1) Vicroy's downburst model could establish the steady-state wind field of the downburst more reasonably when there was only low-level wind speed observation data, and its simulation results were close to the two-dimensional downburst numerical simulation results; (2) Compared with the normal exponential vertical profile of wind speed, the disturbance caused by the front girder of the double-girder gantry crane structure under the downburst wind field was more severe, which increases the probability of the gantry crane overturning. (3) The downwind displacement of the main girder of the gantry crane under the condition of downburst is far greater than that under the normal condition. At the same time, under the condition of downburst, the pressure difference on the surface of the gantry crane was greater, and the distribution of the support reaction force was more uneven, resulting in a stronger overturning tendency of the gantry crane. (4) Under the condition of downburst, the overturning moment and the shearing force borne by the foundation of gantry crane exceeded the critical value to maintain the stability of the gantry crane by the gravity, resulting in the overturning of the gantry crane.

1. Introduction

The Pearl River Delta (PRD) region is a region with the high level of human activity [1], and new buildings and public facilities projects are continuously under construction every year. In such projects, gantry cranes are used extensively as important construction tools. However, large construction machinery is vulnerable to damage due to extreme weather, which has caused heavy losses worldwide [2]. The PRD region has also very active extreme weather [3], especially severe convective weather, which occurs frequently and causes relatively major disasters due to the associated destructive gusts.

Since the gantry tower crane is usually tall and has a large span and its main girder has a large windward area, it is easily damaged

Fig. 1. Time history of average wind speed of a microburst.

when a destructive gust strikes. For example, on April 13, 2016, a gantry collapse accident caused by a squall line occurred in Dongguan, a city in PRD region, causing 18 deaths. In addition, downbursts, which are another type of severe convective weather over a much smaller spatial scale than squall lines, could cause similar accidents. On September 12, 2020, a gantry crane collapsed in Shenzhen, another city in PRD region, resulting in 2 deaths and 6 injuries. After investigations by the Meteorological Bureau of Shenzhen Municipality, it was concluded to have been triggered by a downburst.

Compared with strong convective weather, such as squall lines with a spatial scale of 100 km, downbursts have a smaller spatial scale and a shorter life cycle, and therefore, are more difficult to observe. However, when a downburst occurs, it can easily lead to considerable property and life loss. Considering the safety of aircraft take-off and landing, Fujita [4] first proposed the concept of the downburst. Choi et al. [5,6] analyzed multi-year meteorological observation data in Singapore and Hong Kong and concluded that compared with tropical cyclones and monsoons, the extreme wind speed caused by gusts from strong convective weather, including downbursts, account for a higher proportion of the annual extreme gust wind speed, and the associated frequency and intensity of thunderstorms are notable. Hjelmfelt [7] summarised the characteristics of the structure and the flow field microbursts and pointed out that the experimental phenomenon of wall jets is similar to downbursts.

Because it is not easy to obtain direct observation data, physical simulation and numerical simulation are important methods to study downburst. The results of physical scaled-down simulations show that the impinging jet model is consistent with the full-scale observations [8]. In the past 50 years, computational fluid dynamics (CFD) has been an increasingly established field in urban physics research [9]. Gao et al. [10] investigated the accuracy of CFD simulations for predicting the mean and turbulent wind characteristics around a high-rise building surrounded by low-rise street canyons. Also, CFD simulation helped in analyzing the mechanism of the ventilation performance by visualizing airflow velocity magnitudes [11]. As CFD have been widely used in wind engineering research in recent years, the simulation research of downburst based on CFD has gradually increased. Chay et al. [12] used the k- ε model to study the mean wind field of a downburst while Kim and Hangan [13] used the Reynolds stress model to study the correlation between impinging jet and Reynolds number, as well as its unsteady characteristics.

In all the studies on downburst, describing the vertical distribution of its wind speed is an important task, because it is very important for engineering applications such as wind resistance design. Just as the atmospheric boundary layer wind can be described by the exponential law, the downburst can also be described based on analytical and empirical models. However, many studies have already pointed out that the vertical distribution of wind speed of downburst is significantly different from the exponential or logarithmic wind profile model. Oseguera and Bowles [14] proposed a three-dimensional (3D) steady-state field model in the cylindrical coordinate system, followed by Vicroy [15], who improved the shape function of the wind profile based on the measured data, and put forward the OBV (Oseguera-Bowles-Vicroy) model. Wood et al. [16] fitted the results of the impinging jet test and proposed a steady-state downburst wind profile model. Li et al. [17] integrated the non-linear evolution of the downburst boundary layer into a new shape function and proposed a new wind profile model. Based on the new profile model, the response surface methodology (RSM) model was then used to simulate the 3D static impinging jet, and the numerical simulation results were fitted with the wind speed model.

As mentioned above, a gantry crane collapsed in Shenzhen on September 12, 2020, and downburst was considered as the leading cause. However, in this accident, the maximum wind speed observed by the automatic weather station around the accident site is only about 8 m/s, which is a very common wind speed in this region and is difficult to cause the gantry crane to overturn. Considering that the observation height of the automatic weather station is not high, it may be because the wind speed increases rapidly in the vertical direction, so that at the girder height of the gantry crane, the wind speed exceeds the limitation that the gantry crane can bear, which causes the crane to overturn. In order to analyze the cause of the accident, this paper uses the method of CFD simulation and fluid-structure interaction response analysis to study the physical mechanism of the gantry crane overturning. Through the research, it is expected to improve the scientific understanding of the disaster mechanism of downburst, so as to provide a better basis for preventing the recurrence of similar accidents.
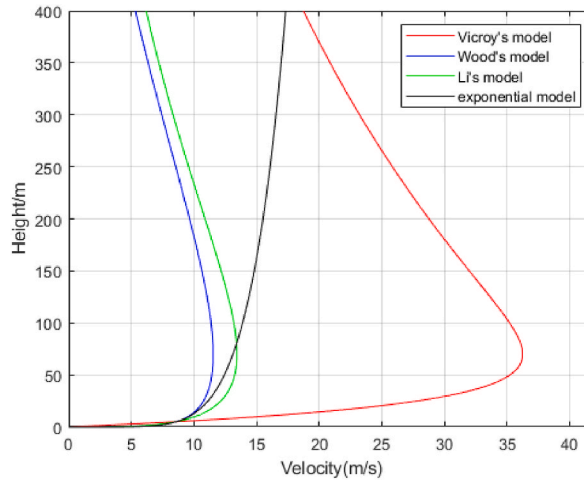
Fig. 2. Comparison of wind profiles of semi-empirical models.

2. Data and methods

2.1. Observation data

Taking the September 12, 2020 Shenzhen gantry crane collapse accident as a case study on the disaster-causing mechanism of downbursts. The accident occurred at a construction site of the Shenzhen West Rail Line 20. The observation data from the Heping automatic weather station (AWS) near the accident site was used in the study. The wind speed sensor of Heping AWS is about 5 m above the surface. The wind speed observation data before and after the accident are shown in Fig. 1. As can be seen from Fig. 1, there is an obvious peak wind speed at about 6pm when the accident occurred, with the maximum wind speed of 8.6 m/s.

2.2. Introduction to the wind profile model

Variations in mean wind speed of conventional boundary layer winds with height can be expressed based on the exponential and logarithmic laws. The calculation accuracy of both expressions does not differ considerably, and the exponential law is convenient for describing the average wind profile of the conventional boundary layer. China's "Load Code for the Design of Building Structures" adopts the exponential law and provides reference values of the roughness index α in different landform environments. The expression of the exponential law is shown in Eq. (1):

$$U(z) = U_r \left(\frac{z}{z_r}\right)^{\alpha} \#$$

(1)

where U(z) is the average wind speed at height z; U_r is the average wind speed at the reference height; z_r is the reference height; α is the ground roughness index. According to the surrounding environment where the September 12, 2020 Shenzhen gantry crane collapse accident occurred, the area is consistent with Class B characteristics of the ground environment and the ground roughness index α is 0.16.

It can be understood that the wind speed obtained by fitting the exponential law model alone is not enough to overturn the gantry crane. Therefore, 3 existing downburst wind speed profile analytical models are further selected, which are Vicroy's, Wood's, and Li's models. The expressions of each model are shown in Eqs. (2)–(4):

Vicroy's model [18]:

$$\frac{U(z)}{U_{max}} = \frac{e^{c_1\left(\frac{z}{z_{max}}\right)} - e^{c_2\left(\frac{z}{z_{max}}\right)}}{e^{c_1} - e^{c_2}} \#$$

(2)

where c_1 and c_2 are empirical constants, Vicroy [15] suggests $c_1 = -0.15$ and $c_2 = -3.2175$; U_{max} is the maximum horizontal wind speed of the downburst; z_{max} is the height of the maximum horizontal wind speed of the downburst, with the maximum wind speed occurring between 50 m and 100 m.

Wood's model [16]:

$$\frac{U(z)}{U_{max}} = A\left(\frac{z}{\delta}\right)^{B} \times \left[1 - \text{erf}\left(\frac{C \cdot z}{\delta}\right)\right] \#$$

(3)

where A, B, and C are empirical constants. Through wind tunnel tests, Wood et al. [16] suggested that A = 1.55, B = 1/6, and C = 0.7; δ
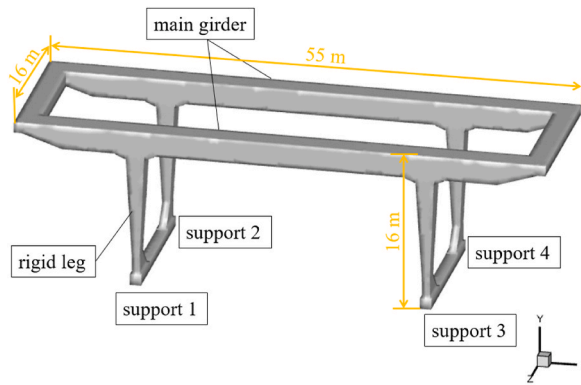
Fig. 3. Finite element model.

is the characteristic height (m) at a half of the maximum radial wind speed.

Li's model [17]:

$$\frac{U(z)}{U_{max}} = \left(\frac{z}{z_{max}}\right)^{\gamma} e^{\gamma\left(1-\frac{z}{z_{max}}\right)} \#$$

(4)

where γ is an empirical constant, and Li et al. [17] found that $\gamma = 0.261$ by fitting the average measured data of downbursts in the NIMROD project [19].

Fujita pointed out that the horizontal wind speed of the downburst increases rapidly with height in the near-surface area to a maximum value, and then decreases rapidly. The maximum wind speed occurs at a height of about 50–100 m [20]. Therefore, when selecting the height parameter where the maximum wind speed is located, $z_{max} = 70$ m was selected according to the previous values in the reference. Combining the near-surface wind speed data observed by the Heping AWS and formulas (2) to (4), the maximum wind speeds of the three models can be obtained as 36.3, 11.5, and 13.4 m/s, respectively. Fig. 2 compares the wind speed vertical profile obtained by the three models with the profile calculated by the exponential law model of formula (1). It can be seen from Fig. 2 that the maximum wind speeds obtained from the Wood's model and the Li's model are much weaker than expected, and the maximum wind speed in the boundary layer derived from the observed wind speed is not more than 15 m/s, which is a wind speed frequently observed in this region and is far from enough to overturn a gantry crane. While the wind speed derived from the Vicroy's model is far greater than that of the other two models, and also greater than that derived from the exponential law model. The wind speed at the height of 70 *m* exceeds force 12, which is quite destructive enough to overturn a gantry crane. Therefore, the study in the following sections will focus on the Vicroy's model.

2.3. Numerical calculation model of two-dimensional downburst wind field

When the observation data is limited, it is an alternative and feasible way to verify with the results of idealized numerical simulation. In the current study, in order to verify the reliability of the Vicroy's model, a 2D impinging jet model was used to simulate the process of downburst, and the simulated vertical profile of wind speed is compared with the results obtained by using the Vicroy's model. The jet diameter D was set as 1200 *m*, the jet velocity was 36 m/s, the horizontal scale of the flow field was 12D, the vertical scale was 3D, and the outlet was 2D from the ground. The downburst is an incompressible turbulent flow process, and the numerical governing equation [21] is shown in Eqs. (5) and (6):

$$\frac{\partial \rho}{\partial t} + \frac{\partial \rho u_i}{\partial x_i} = 0 \#$$

(5)

$$\frac{\partial \rho u_i}{\partial t} + \frac{\partial \rho u_i u_j}{\partial x_j} = -\frac{\partial p}{\partial x_i} + \frac{\partial}{\partial x_i}\left[(\mu + \mu_i)\left(\frac{\partial u_i}{\partial x_j} + \frac{\partial u_j}{\partial x_i}\right)\right]\#$$

(6)

where t is time; u_i and u_j are velocity components; x_i and x_j are coordinates; p is pressure; μ is molecular viscosity; μ_i is turbulent viscosity. The k-ω model, which can simulate the flow, separation, and transition of the boundary layer well, was used for the simulation of the downburst radial wind speed. The transient solution adopted the SIMPLE algorithm, while the discretisation format adopts the second-order upwind scheme, and y+ = 100 was selected for near-ground grid refinement.

2.4. Fluid–solid coupling calculation model and grid division

For the fluid–solid coupling simulation, based on the similarity laws of structural dynamic characteristics and the size parameters of
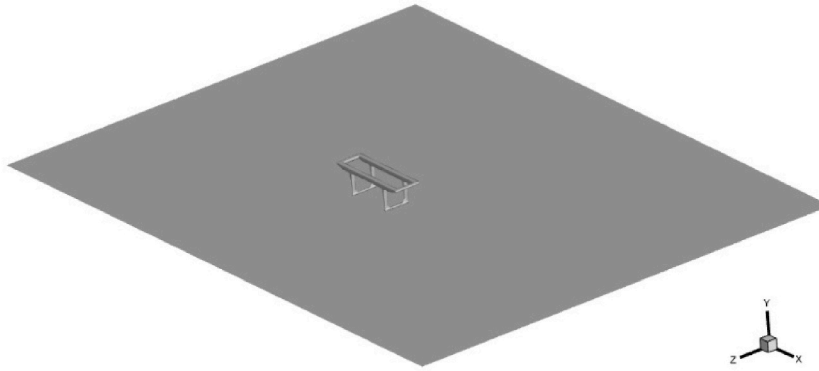
Fig. 4. Computational domain.
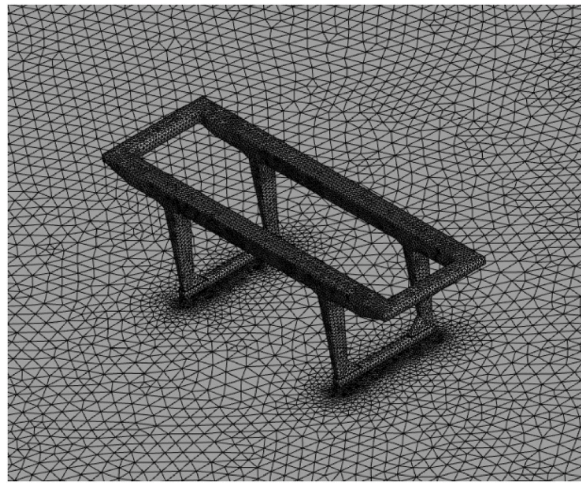
Fig. 5. Mesh division.

structural characteristics, a finite element solid model with the same shape as the gantry crane plates and shells, and the same mass, volume, and vibration mode, was established. The response of the structure and the corresponding flow field characteristics were obtained by fluid-solid coupling analysis.

As this paper studies a strong wind case, the changes of fluid temperature and density are ignored in the simulation. In the fluid-solid interaction response analysis, the length of the main girder of the gantry crane was set as 55 m, and the height as 16 m. The model of the gantry crane is shown in Fig. 3, and the area of fluid-structure coupling numerical simulation is shown in Fig. 4. In the fluid–solid coupling simulation model, the upstream inlet boundary is 3L away from the gantry crane (L is the length of the main girder of the gantry crane), and the length of the downstream area was 4L. The total height was 3H (H is the height of the gantry crane), the span wise length of the left and right sides was 3L. The surface in contact with the solid structure and the fluid in the calculation domain was set as "system coupling", and the dynamic mesh update adopted the smoothing and remeshing methods.

The fluid domain and the solid structure were meshed separately. For the fluid domain, due to the complexity of the gantry crane model, a flexible tetrahedron grid was used. The grid was refined in the vicinity of the model and in the area where the fluid changed significantly. The grid scale on the surface of the model was 0.5 m; the grid division method is shown in Fig. 5. The total number of volume meshes was around 1.47 million.

For the solid structure, the structure of the gantry crane is mainly composed of main girders and outriggers and is usually modelled after its plate and shell elements. However, negative grids are easily generated in the wind field model, whereas the fluid–solid coupling data is only transmitted on the surface of the structure, and the structure of the gantry crane is a complex closed model. To facilitate the establishment of the coupling surface between the fluid and the solid and improve calculation efficiency while retaining structural modal characteristics, the internal structure was ignored during the modelling process and the structure was simplified. Based on the similitude theory of structural dynamics, a 1:1 finite element model with the same shape as the gantry crane plates and shells was established through model fitting, and the structure was constructed as a homogeneous equivalent model with the same mass, volume, and vibration characteristics. The overall mass of the finite element model of the crane was 1.09×10^5 kg, its volume was 925.74 m^3, its density was 117.85 kg/m^3, its elastic modulus was 6978 MPa, and the Poisson's ratio was 0.3.

(a) t=50 s

(b) t=100 s

(c) t=130 s

(d) t=205 s
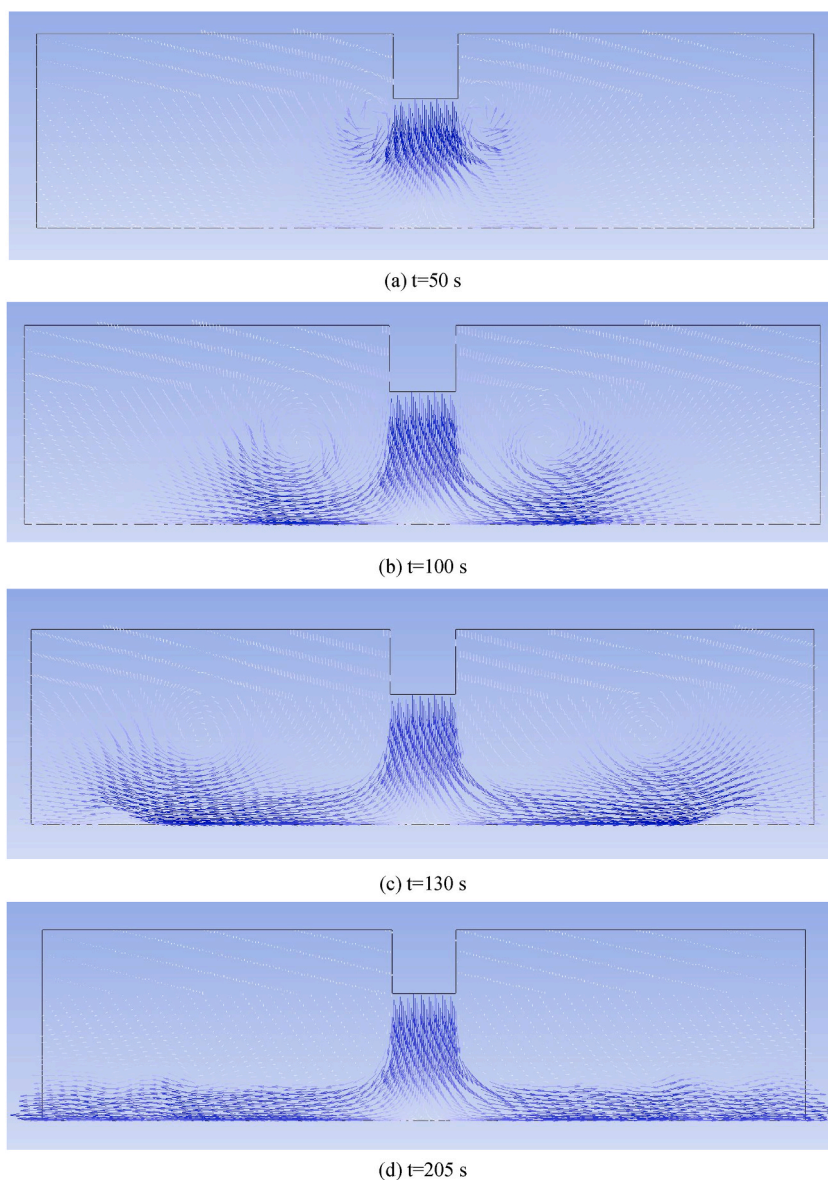
Fig. 6. Velocity vector diagrams of downburst development process.

2.5. Boundary condition setting

There are two models for the wind speed at the inlet boundary, one is the normal exponential law model, the other is the Vicroy's downburst model, and the turbulence intensity at the inlet boundary is 5%. The outflow boundary condition is set for the downstream outlet boundary. The ground and the crane surface adopted the non-slip boundary condition (Non-slip Wall); while the left and right sides and the top surface of the fluid domain adopted the symmetrical boundary condition. The realisable k–ε model was selected for turbulence closure, which has high accuracy in solving the external flow characteristics at high Reynolds numbers [22,23].

For the structural dynamic response calculation module, the four surfaces (supports 1–4) corresponding to the bottom surface of the lower girder of the structural finite element model and the support of the travelling mechanism of the cart were set as 3-directional fixed support. The other surfaces of the crane model, excluding the constraint surface, were set as fluid solid interfaces, and gravity was applied using Standard Earth Gravity setting.

FLUENT software was used in the simulation. Three-dimensional double precision solver was used for the wind field, and the air model used was an incompressible model. Based on the pressure solver and transient time setting selected, the pressure–velocity decoupling adopted the Simple algorithm, and the momentum equation, turbulent kinetic energy and turbulent kinetic energy dissipation rate equation adopted second-order discrete scheme. The convergence standard of iterative calculation was that all
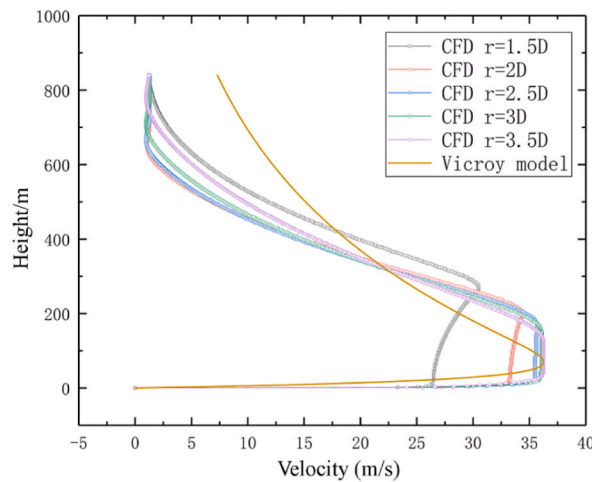
Fig. 7. Comparison of simulation results and semi-empirical model.

Table 1
Comparison of natural vibration characteristics between the plate and shell model and the simplified model.

Order	Plate and shell model frequency (Hz)	Simplified model frequency (Hz)	Error	Vibration mode
1	2.7272	2.7281	0.03%	The whole machine vibrates along the direction of the cart track
2	2.8405	3.0422	7.10%	The whole machine vibrates along the direction of the trolley track
3	3.0186	3.4584	14.57%	Both ends of the main girder vibrate along the cart track in opposite directions
4	4.9793	4.9612	0.36%	The two main girders vibrate along the cart track in opposite directions

variables and dimensionless residuals were below 10^{-4}. The time step was set to 0.01 s, the maximum number of iterations in a single time step was 60, and the total iteration time (End Time) was 5 s. Data transmission was established on the crane surface of the fluid part and the fluid–solid coupling surface of the solid part. In the calculation sequence, the fluid part was calculated first, followed by the solid part.

3. Validation of wind speed profile models

3.1. Simulation of 2D downburst wind field

The evolution of wind field obtained by two-dimensional downburst simulation is shown in Fig. 6. It can be seen from Fig. 6(a–d) that the area with high turbulent kinetic energy at the jet front formed the main annular vortex, which fell off and generated a secondary vortex after impacting the ground. As the main annular vortex moved radially and entered the impact area, the flow field began to stabilise. After stabilisation, the velocity first increased and then decreased in the vertical direction, and there was a more obvious velocity gradient. The simulation results of this model are similar to those of Chay et al. [12], and also generally consistent with the physical image of downburst given by Shehata et al. [8].

3.2. Comparison of models

After the 2D simulation was steady, the vertical profile of wind speed at the radial distance from 1.5D to 3.5D from the outflow was compared with the Vicroy's model, as shown in Fig. 7. It can be found from Fig. 7 that the numerical simulation results were in good agreement with the Vicroy's model, especially in the focused near-surface layer below 100 m in this study, which provides confidence for the further application of the Vicroy's model to the numerical simulation analysis of fluid-structure coupling simulation.

4. Analysis of fluid–structure interaction response

4.1. Modal analysis

The investigation of the simulation results on the natural vibration characteristics of the gantry crane is an important basis for judging the effectiveness of the fluid-structure coupling simulation. Therefore, modal analysis is carried out on the gantry crane plate

(a)

(b)
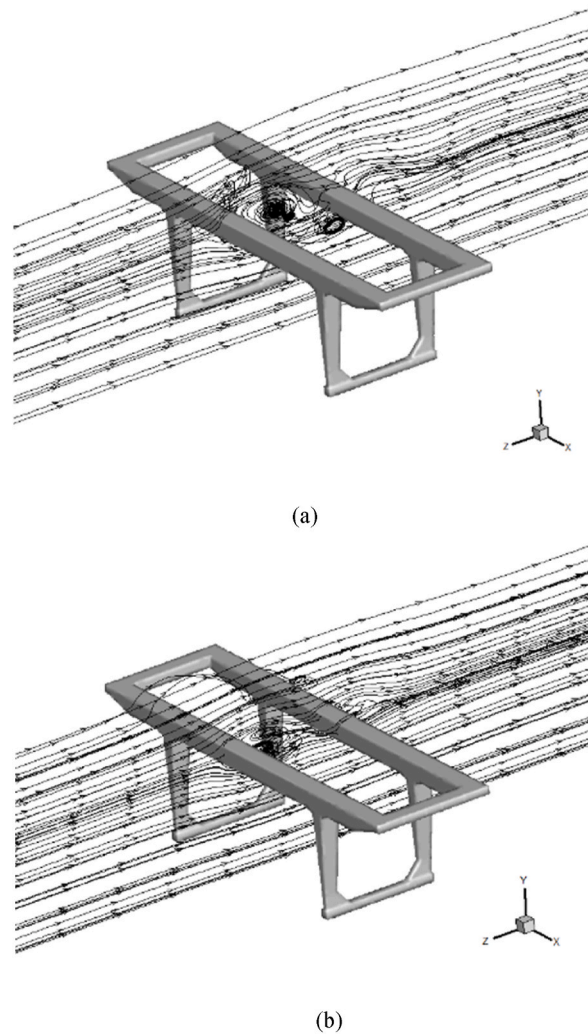
Fig. 8. Streamline diagram of downburst (a) and exponential wind (b).

and shell structure model and the homogeneous equivalent model obtained by modal fitting. The first four natural frequencies were compared, with the results listed in Table 1. The gap between the homogeneous equivalent model of the gantry crane and the plate and shell structure model was within 15% (Table 1), indicating that the established homogeneous equivalent model fit well with the plate and shell structure model, and could be equivalently applied to fluid–structure interaction response analysis.

4.2. Flow field analysis

Fig. 8 illustrates the wind field around the gantry crane simulated by using different boundary inflow profiles according two different models, namely, the Vicroy's model (Fig. 8(a)) and the exponential law model (Fig. 8(b)).

Both the downburst wind field and the exponential boundary layer wind field reflected flow field characteristics of classic blunt body turbulence. Under the two boundary profile conditions, flow separation of the upper and lower sides of the front girder of the gantry crane occurred, and a wake vortex was generated at the leeward side of the front girder. The difference was that in the downburst wind field, the wake area at the rear end of the front girder was wider and the disturbance was more intense, which also indicated that the probability of the gantry crane overturning increases under the impact of downburst.

It can also be found that the flow field on the upwind side of the front girder does not have as severe disturbances as on the downwind side, which means that the upwind side geometric size of the simulation domain can be reduced, thereby reducing the computational resources required for simulation.

4.3. Analysis of wind load and structural response

The pressure distribution simulated by using the two boundary profiles conditions is shown in Fig. 9. After the incoming flow
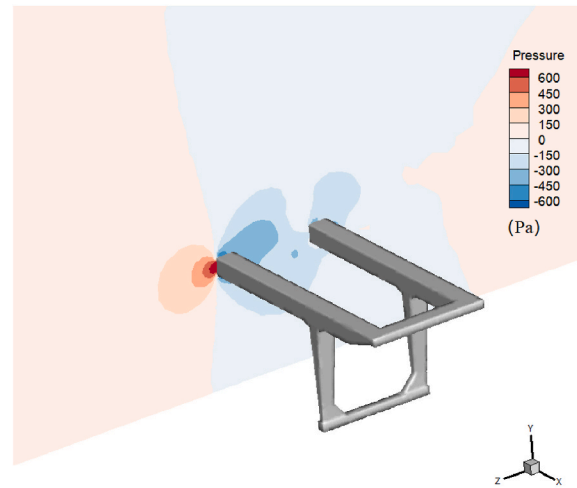
(a)
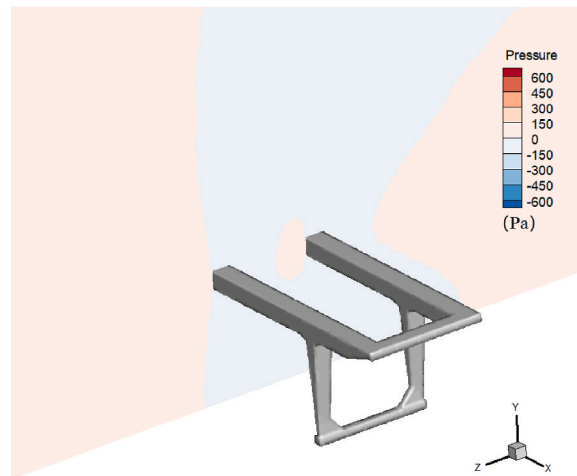
(b)

Fig. 9. Pressure distribution of downburst (a) and exponential wind (b) profiles at x = 0.

separated from the front girder, a large negative pressure area was generated at the leeward side of the front girder, and the wind pressure on the windward side of the rear girder decreased. The upstream structure produced a clear shielding effect on the downstream. Under the downburst wind field (Fig. 9(a)), the wake vortex formed by the front girder was larger and the separated fluid did not attach to the rear girder; thus, the front end of the rear girder also exhibited negative pressure, with greater negative pressure at the leeward side of the rear girder. This is inconsistent with the positive value of the pressure on the windward side of the rear girder under the condition of the exponential-law wind (Fig. 9(b)), which was mainly caused by the different ranges of influence of the wake vortex. Furthermore, under the downburst condition, the difference between positive pressure and negative pressure is greater than that under the exponential-law wind condition, which means that the gantry crane bears more pressure under the downburst condition.

Fig. 10 shows the surface pressure distribution of the gantry crane under the two wind profile conditions. By interacting with structures, the wind generates pressure differences between upwind and downwind facades [24], so there was a strong positive pressure on the windward surface of the gantry crane and a negative pressure on the lateral boundary and lee side of the gantry crane due to the separation of the flow. The maximum positive wind pressure on the windward surface under the condition of the downburst (Fig. 10(a)) was 814.8 Pa, which was greater than the maximum positive pressure of 120.0 Pa obtained by the exponential-law wind (Fig. 10(b)), indicating that the surface pressure of the gantry crane varied greatly under different wind fields. Through the two-way

(a)

(b)
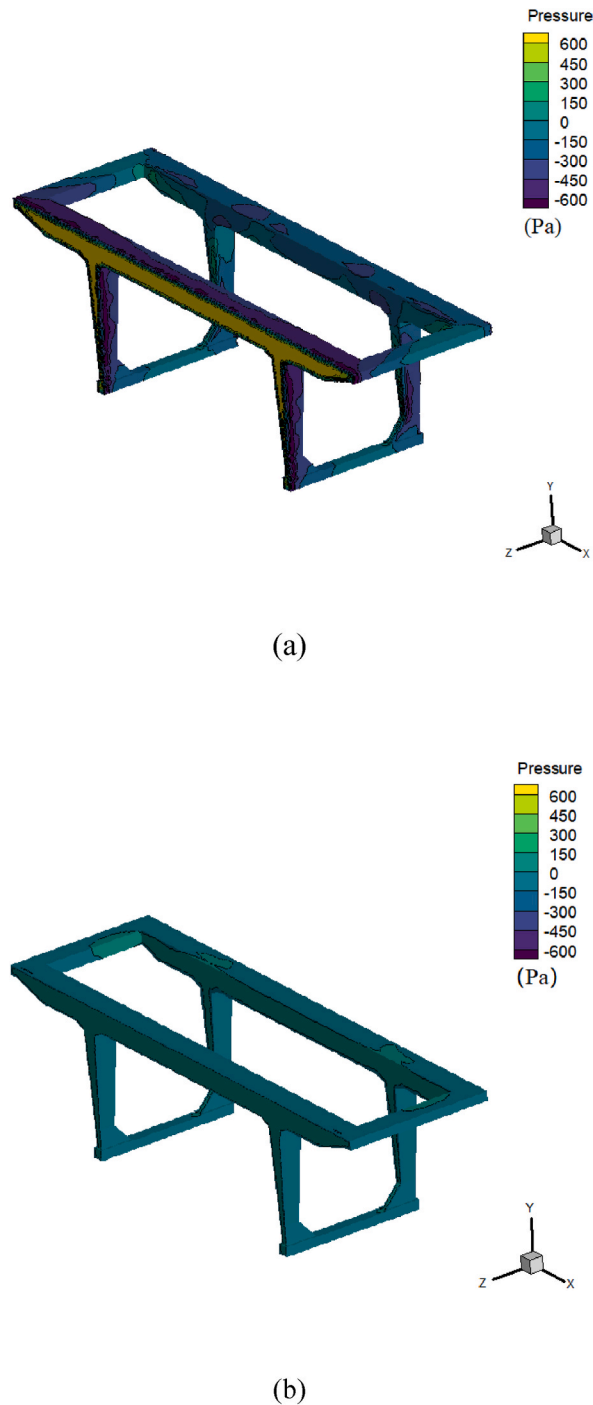
Fig. 10. Surface pressure distribution of gantry crane under the action of downburst (a) and exponential wind (b).

fluid–solid coupling calculation, the maximum displacement of the gantry crane in the downwind direction under the condition of the downburst was derived as 12.78 mm, which was greater than that of the exponential-law wind, 2.13 mm. Considering that the two wind profile conditions have the same wind speed of 8.6 m/s at a height of 5 *m* above the ground, the significant difference between the wind pressure and the shape displacement of the gantry crane is enough to explain that the special wind field structure of downburst may have a huge impact on the towering large-span structure such as the gantry crane.

On-site investigations showed that gantry crane accidents caused related to strong wind were generally caused by the sliding and overturning of the gantry crane along the travelling direction of the cart [25] Whether the gantry crane has a tendency of slipping or

Table 2
Crane support reaction force values under different wind fields.

Support	Direction	Support reaction force of Vicroy's model ($\times 10^5$N)	Support reaction force of exponential model ($\times 10^5$N)
1	Vertical	2.159	2.587
	Horizontal	0.142	0.048
2	Vertical	2.159	2.587
	Horizontal	0.145	0.048
3	Vertical	3.182	2.746
	Horizontal	0.181	0.177
4	Vertical	3.185	2.745
	Horizontal	0.180	0.177

overturning can be evaluated based on the value of the support reaction force at the bottom of the gantry crane. Table 2 shows the support reaction force values of each support under each wind field. Differences in the vertical support reaction forces of the four supports under the action of exponential-law wind were small, while that of supports 1 and 2 and supports 3 and 4 under the downburst were relatively large (Table 2). The results demonstrate that the distribution of the reaction force of the structure under the downburst flow was very uneven. At the same time, under the condition of downburst, the horizontal support reaction force on the four supports of the gantry crane was also significantly greater than that under the condition of the exponential-law wind, indicating that the gantry crane had a greater tendency to slip. Therefore, compared with the exponential law wind profile condition, the gantry crane under downburst condition has a greater tendency to both overturn and slip, which means that the probability of damage of the gantry crane is much higher.

Furthermore, the moment of the gantry crane under two wind conditions is also calculated. The overturning moment of the gantry crane under exponential-law wind is 3.42×10^5 N m, and the that under the downburst condition is 2.31×10^6 N m. According to the gravity borne by the gantry crane itself, the critical value of the moment to maintain stability can be calculated as 8.54×10^5 N m. Therefore, the anti-overturning stability of gantry crane under exponential-law wind conditions meets the requirements. While, under the condition of downburst, the wind-leading overturning moment of the gantry crane is 2.7 times of the critical value of the moment to maintain stability, and the gantry crane will overturn.

For the anti-sliding stability of the gantry crane, the shearing force of the gantry crane base under two wind conditions is calculated, and the shearing force on the gantry crane base under the exponential-law wind condition is 25.19 kN, while the shearing force of the gantry crane calculated under the downburst condition is 174.42 kN. If all wind-proof equipment fails to work, the resistance of the gantry crane in the travelling direction of the support pulley is mainly provided by friction. According to the Chinese National Standard for Design of Cranes (GB/T3811-2008), the friction coefficient between the rail and the pulley is 0.14, so the gantry crane can provide 137.2 kN friction resistance by its own gravity. Therefore, the gantry crane will not slip under the condition of exponential-law wind condition, while the friction resistance alone is not enough to prevent the sliding under the condition of downburst.

> To sum up, under the condition of downburst, the wind pressure, support reaction, overturning moment and shearing force borne by the gantry crane are far greater than those under the condition of exponential-law wind profile, and the overturning moment and base shear force also exceed the critical value that can maintain stability by relying on the gravity of the gantry crane, resulting in the overturning and damage of the gantry crane.

5. Conclusion

Based on the fluid–solid coupling simulation with a semi-empirical model of the wind profile and measured data, the wind load characteristics of the gantry crane under the condition of the downburst were studied. The findings indicated the following:

(1) Compared with Wood's and Li's model, the Vicroy's model could establish the vertical profile of downburst wind more reasonably when there was only low-altitude wind speed observational data. There is a significant difference between the downburst wind vertical profile and the normal exponential-law wind profile, and the wind speed increases sharply with height and forms a strong low-level jet in the near-surface layer during the downburst.

(2) Compared with the normal exponential-law wind, the disturbance caused by the front girder of the gantry crane under the downburst condition is more severe, and the probability of the gantry crane overturning increases. The downwind displacement of the gantry crane under the condition of downburst is far greater than that under the condition of exponential-law wind. At the same time, under the condition of downburst, the surface pressure of the gantry crane is very different, and the distribution of the support reaction is more uneven, which makes the gantry crane have a much stronger tendency to overturn.

Author contribution statement

Jia-Chen Su: Conceived and designed the experiments; Performed the experiments; Analyzed and interpreted the data; Wrote the paper. Lei Li: Conceived and designed the experiments; Contributed reagents, materials, analysis tools or data; Wrote the paper. Pak Wai Chan: Contributed reagents, materials, analysis tools or data; Wrote the paper. Qian-Jin Zhou: Analyzed and interpreted the data. Hong-Long Yang: Contributed reagents, materials, analysis tools or data.

Data availability statement

The authors do not have permission to share data.

Declaration of competing interest

The authors declare that they have no known competing financial interests or personal relationships that could have appeared to influence the work reported in this paper.

References

[1] L. Sun, J. Chen, Q. Li, D. Huang, Dramatic uneven urbanization of large cities throughout the world in recent decades, Nat. Commun. 11 (2020) 5366.
[2] Y. Takefuji, How to build disaster-resilient cities and societies for making people happy, Build. Environ. 228 (2023), 109845.
[3] L. Li, P.W. Chan, T. Deng, H.-L. Yang, H.-Y. Luo, D. Xia, Y.-Q. He, Review of advances in urban climate study in the Guangdong-Hong Kong-Macau greater bay area, China, Atmos. Res. 261 (2021), 105759.
[4] T.T. Fujita, Manual of Downburst Identification for Project NIMROD, 1978. https://ntrs.nasa.gov/citations/19780022828. accessed November 6, 2022.
[5] E.C.C. Choi, H.Y. Mok, T. Lee, Occurrence and Significance of Thunderstorms in Hong Kong, 2007.
[6] E.C.C. Choi, A. Tanurdjaja, Extreme wind studies in Singapore. An area with mixed weather system, J. Wind Eng. Ind. Aerod. 90 (2002) 1611–1630.
[7] M.R. Hjelmfelt, Structure and life cycle of microburst outflows observed in Colorado, J. Appl. Meteorol. Climatol. 27 (1988) 900–927.
[8] A.Y. Shehata, A.A. El Damatty, E. Savory, Finite element modeling of transmission line under downburst wind loading, Finite Elem. Anal. Des. 42 (2005) 71–89.
[9] B. Blocken, Computational Fluid Dynamics for urban physics: importance, scales, possibilities, limitations and ten tips and tricks towards accurate and reliable simulations, Build. Environ. 91 (2015) 219–245.
[10] H. Gao, J. Liu, P. Lin, C. Li, Y. Xiao, G. Hu, Pedestrian level wind flow field of elevated tall buildings with dense tandem arrangement, Build. Environ. 226 (2022), 109745.
[11] Y. He, Y. Chu, H. Zang, J. Zhao, Y. Song, Experimental and CFD study of ventilation performance enhanced by roof window and mechanical ventilation system with different design strategies, Build. Environ. 224 (2022), 109566.
[12] M.T. Chay, F. Albermani, R. Wilson, Numerical and analytical simulation of downburst wind loads, Eng. Struct. 28 (2006) 240–254.
[13] J. Kim, H. Hangan, Numerical simulations of impinging jets with application to downbursts, J. Wind Eng. Ind. Aerod. 95 (2007) 279–298.
[14] R.M. Oseguera, R.L. Bowles, A Simple, Analytic 3-dimensional Downburst Model Based on Boundary Layer Stagnation Flow, 1988. https://ntrs.nasa.gov/citations/19880018674. accessed November 6, 2022.
[15] D.D. Vicroy, Assessment of microburst models for downdraft estimation, J. Aircraft 29 (1992) 1043–1048.
[16] G.S. Wood, K.C.S. Kwok, N.A. Motteram, D.F. Fletcher, Physical and numerical modelling of thunderstorm downbursts, J. Wind Eng. Ind. Aerod. 89 (2001) 535–552.
[17] C. Li, Q.S. Li, Y.Q. Xiao, J.P. Ou, A revised empirical model and CFD simulations for 3D axisymmetric steady-state flows of downbursts and impinging jets, J. Wind Eng. Ind. Aerod. 102 (2012) 48–60.
[18] D.D. Vicroy, A Simple, Analytical, Axisymmetric Microburst Model for Downdraft Estimation, National Aeronautics and Space Administration, Langley Research Center, 1991.
[19] T.T. Fujita, The Downburst, Report of Projects NIMROD and JAWS, Chic. Univ. Chic., 1985.
[20] T.T. Fujita, Tornadoes and downbursts in the context of generalized planetary scales, J. Atmos. Sci. 38 (1981) 1511–1534.
[21] F. Magoules, Computational Fluid Dynamics, CRC Press, 2011.
[22] L. Li, F. Hu, X.L. Cheng, H.Y. Han, The application of computational fluid dynamics to pedestrian level wind safety problem induced by high-rise buildings, Chin. Phys. 13 (2004) 1070–1075.
[23] L. Li, F. Hu, X.L. Cheng, J.H. Jiang, X.G. Ma, Numerical simulation of the flow within and over an intersection model with Reynolds-averaged Navier-Stokes method, Chin. Phys. 15 (2006) 149–155.
[24] H. Montazeri, B. Blocken, CFD simulation of wind-induced pressure coefficients on buildings with and without balconies: validation and sensitivity analysis, Build. Environ. 60 (2013) 137–149.
[25] F. Frendo, Gantry crane derailment and collapse induced by wind load, Eng. Fail. Anal. 66 (2016) 479–488.